

## SUBARCSECOND MID-INFRARED IMAGING OF DUST IN THE BIPOLAR NEBULA HEN 3-401<sup>1</sup>

C. MUTHUMARIAPPAN

Institute of Astronomy and Astrophysics, Academia Sinica, Taipei 10617, Taiwan; muthu@asiaa.sinica.edu.tw

SUN KWOK

Institute of Astronomy and Astrophysics, Academia Sinica, Taipei 10617, Taiwan; and Department of Physics and Astronomy, University of Calgary, Calgary, AB, Canada; kwok@asiaa.sinica.edu.tw

AND

KEVIN VOLK

Gemini Observatory, Hilo, HI 96720; kvolk@gemini.edu

Received 2005 August 8; accepted 2005 November 18

### ABSTRACT

We present high-resolution, nearly diffraction-limited narrow- and broadband mid-IR images of bipolar reflection nebula Hen 3-401. The deconvolved images yield a pixel-limited spatial resolution of  $0''.09$ , demonstrating the superior imaging quality of the Gemini telescope. The infrared image of Hen 3-401 consists of a prominent core region of size  $1''$  and extended emissions along the walls of the bipolar lobes. We find that the distribution of aromatic infrared band (AIB) emission is different from that of the continuum emission and that the star has undergone multiple ejection of the AIB emission feature carrier at the end stages of its evolution. From the observed temperature gradient in the core, we suggest that the core has a flared disk geometry.

*Subject headings:* planetary nebulae: general — stars: AGB and post-AGB — stars: emission-line, Be

### 1. INTRODUCTION

Hen 3-401 (IRAS 10178–5958, SS73 21, Wray 15-543) is an emission nebula first discovered in the emission-line surveys of the southern skies by Henize (1976) and Sanduleak & Stephenson (1973). It was found to possess large infrared excesses similar to those observed in planetary nebulae (PNs) by *IRAS* (Parthasarathy & Pottasch 1989). High-resolution images obtained with the WFPC2 camera on board the *Hubble Space Telescope* (*HST*) revealed a highly collimated bipolar outflow (Sahai et al. 1999). Two very long, cylindrical, bipolar lobes of length  $14''.5$  are seen in reflection light with an aspect ratio of about 7, suggesting that the bipolar lobes were created by a highly collimated outflow. The *HST* images also show the presence of an equatorial torus (dark lane) and a bipolar skirtlike structure, both coaxial with the lobes, and also a faint halo around the lobes. The lobes have unequal surface brightness and are separated by a dark dust lane (Sahai et al. 1999). The presence of a circumstellar disk is also supported by the observation of a circular polarization pattern (Scarrott & Scarrott 1995). The star in Hen 3-401 has a spectral type of Be, so it has been suggested as a candidate proto-planetary nebula (PPN), but observationally speaking, it is more accurate to describe Hen 3-401 as a bipolar nebula illuminated by a central star of temperature  $\sim 22,000$  K. Many symbiotic stars also have a strong infrared excess and bipolar structure, but their central stars are not evolving rapidly to the planetary nebula stage (Corradi 2003; Kwok 2003). Hen 3-401 may belong to the class of bipolar objects containing M2-9, Min 1-92, Hen 2-104, Mz 3 (PN G331.7 – 01.0), etc., whose evolutionary status is uncertain.

In addition to the large infrared excess, Hen 3-401 also shows strong  $H_2$  emission (García-Lario et al. 1999). Strong aromatic infrared bands (AIBs) seen in its *Infrared Space Observatory* (*ISO*) Short Wavelength Spectrometer (SWS) spectrum suggest that the object is carbon-rich (Parthasarathy et al. 2001). Its carbon-rich nature is also supported by the detection of CO millimeter emission lines (Bujarrabal & Bachiller 1991; Loup et al. 1993) and the absence of any OH maser emission at 1612 MHz (Silva et al. 1993). With the advent of large-aperture telescopes optimized for the thermal infrared observations, it has now become possible to obtain subarcsecond resolution mid-infrared images of the dust shells of PPNs (Kwok et al. 2002). In this paper we report mid-infrared imaging of Hen 3-401 using the 8 m Gemini South telescope.

### 2. OBSERVATIONS AND DATA REDUCTION

Mid-infrared imaging observations of Hen 3-401 were made on 2003 December 30 under program GS-2003B-Q-23, with the Thermal Region Camera Spectrograph (T-ReCS) mounted at the 8 m Gemini South telescope. T-ReCS is a mid-infrared imager and long-slit spectrograph built by the University of Florida for Gemini South. It employs a Raytheon Si:As Impurity-band Conductor (IBC) array having a  $320 \times 240$  pixel format, with pixel scale of  $0''.09$  and a field of view of  $28''.8 \times 21''.6$ . The instrument design is optimized for low thermal background, high throughput, and excellent image quality in the mid-infrared wavelength region between 8 and  $26 \mu\text{m}$ , to take advantage of the high thermal-infrared performance of the Gemini telescopes. T-ReCS, combined with Gemini's fast tip/tilt compensating secondary mirror, yields nearly diffraction-limited images under most natural seeing conditions. The diffraction-limited spatial resolution of T-ReCS at  $10 \mu\text{m}$  is  $\sim 0''.4$ .

Imaging observations were carried out with broad and medium bandpass filters in the *N* and *Q* bands, namely, Si-4 (central wavelength  $\lambda_0 = 10.38 \mu\text{m}$ , bandwidth  $\Delta\lambda = 1.02 \mu\text{m}$ ), Si-5 ( $\lambda_0 = 11.66 \mu\text{m}$ ,  $\Delta\lambda = 1.13 \mu\text{m}$ ), Si-6 ( $\lambda_0 = 12.33 \mu\text{m}$ ,  $\Delta\lambda = 1.18 \mu\text{m}$ ),

<sup>1</sup> This paper is based on observations obtained at the Gemini Observatory, which is operated by the Association of Universities for Research in Astronomy, Inc., under a cooperative agreement with the NSF on behalf of the Gemini partnership: the National Science Foundation (US), the Particle Physics and Astronomy Research Council (UK), the National Research Council (Canada), CONICYT (Chile), the Australian Research Council (Australia), CNPq (Brazil), and CONICET (Argentina).

TABLE 1  
MEASURED FLUXES AT DIFFERENT FILTERS

$\lambda$ ( $\mu\text{m}$ )	On-Source Time (s)	Flux in the Core (Jy)	Flux in the Lobes (Jy)	Total Flux (Jy)	PSF Size (arcsec)
10.36.....	260.6	3.62	0.71	4.33	0.382
10.38.....	260.6	2.53	0.54	3.07	0.365
11.66.....	260.6	3.17	0.63	3.80	0.369
12.33.....	260.6	3.78	0.43	4.21	0.427
18.30.....	260.6	7.61	8.82	16.43	0.564
24.56 <sup>a</sup> .....	248.3	9.40	30.42	39.82	0.700

<sup>a</sup> T-ReCS flux was scaled using the *ISO* SWS flux.

N ( $\lambda_0 = 10.36 \mu\text{m}$ ,  $\Delta\lambda = 5.27 \mu\text{m}$ ), Qa ( $\lambda_0 = 18.30 \mu\text{m}$ ,  $\Delta\lambda = 1.51 \mu\text{m}$ ), and Qb ( $\lambda_0 = 24.56 \mu\text{m}$ ,  $\Delta\lambda = 1.92 \mu\text{m}$ ). Standard star observations were made for each filter to determine the point-spread function (PSF) as well as for flux calibration. The observing log is given in Table 1.

Accurate cancellation of the mid-infrared sky and telescope background radiation was obtained by the usual technique of chopping and nodding. The secondary mirror is capable of two-point (square wave) chopping at an arbitrary position angle on the sky, with the chop frequency of  $\sim 3$  Hz and an amplitude of up to  $\pm 7''.5$  (the maximum chopper throw is  $15''$ , which is considerably smaller than the T-ReCS field of view). The observations were taken in an ABABABAB nodding pattern. The raw data was stored in a multiple extension FITS (MEF) format file, with one extension for each NOD position, and with typically three image samples per NOD position. Multiple frames were co-added to produce each output image, with a frame integration time of 7.97 ms for the Qb filter and 25.86 ms for the other filters. The MEF images were stacked and reduced with the standard pipeline reduction task `mirreduce`, in the Gemini IRAF package.<sup>2</sup> The reduced data were then subjected to photometric calibration using the accompanying standard star observations. For this purpose the absolute fluxes

<sup>2</sup> IRAF is distributed by the National Optical Astronomy Observatory, which is operated by the Association of Universities for Research in Astronomy, Inc., under cooperative agreement with the National Science Foundation.

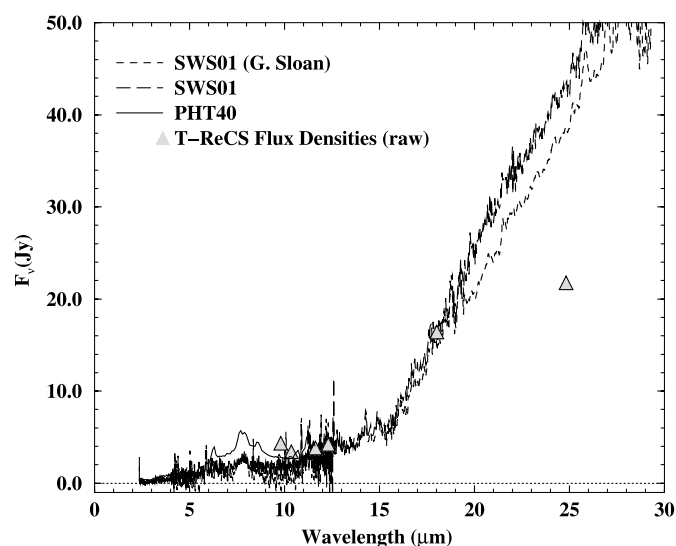


FIG. 1.—T-ReCS fluxes measured at different filters are shown with the *ISO* SWS spectra of Hen 3-401. The SWS01 spectrum labeled G. Sloan was provided by G. Sloan. The unlabeled one was processed by K. V.

of the calibration star  $\alpha$  CMa were taken from Cohen et al. (1999). The spectral energy distribution (SED) was integrated over the filter profiles, weighted by photon number.

The reduced T-ReCS images were then deconvolved using the PSF images of  $\alpha$  CMa. We have adopted the Lucy deconvolution algorithm, available in IRAF, and the deconvolved images were subsequently smoothed with a  $2 \times 2$  pixel box to improve the signal-to-noise ratio (S/N). The final spatial resolution for these images is  $0''.18$ .

The total fluxes for the different T-ReCS filters are given in Table 1. These measurements are not corrected for the differential atmospheric extinction with the standard star  $\alpha$  CMa (the difference in air mass was small, so these corrections are not generally expected to be large for most of these filters). These flux values plotted against two different reductions of the SWS spectrum of Hen 3-401 are shown in Figure 1, which demonstrates that ground-based mid-IR flux measurements are in good agreement with the space measurements, except for the  $24 \mu\text{m}$  filter. That particular filter is known to be the most sensitive to changes in atmospheric conditions of all the T-ReCS filters.

### 3. RESULTS

Figure 2 shows the Gemini mid-IR images (*contours*) superimposed on an *HST* image (*gray scale*) taken with 606W filter. As the T-ReCS images are not taken with good astrometry, the matching of coordinates was done by locating the dust features at shorter wavelengths (from *HST* NICMOS images). The (0, 0) position in Figure 2 is R.A. =  $10^{\text{h}}19^{\text{m}}32^{\text{s}}.47$ , decl. =  $-60^{\circ}13'29''.4$  (J2000). Although the images have been smoothed over  $2 \times 2$  pixels, the intensity contours are expressed in units of mJy per pixel. To convert the intensity scale to per  $\text{arcsec}^2$ , we need to multiply the values by 124.34. For example,  $10 \text{ mJy pixel}^{-1}$  would correspond to  $1.24 \text{ Jy arcsec}^{-2}$ .

The T-ReCS images show that the mid-IR emission is enhanced in the circular core of diameter  $1''$ ; around 75% of the total flux at  $10 \mu\text{m}$  and 58% at  $20 \mu\text{m}$  is emitted from this region. The emission is extended along the polar regions and distributed mostly along the bipolar walls (similar to the optical morphology in scattered light), implying that the radiation is limb brightened, and hence it is optically thin at mid-IR wavelengths. There is no emission detected along the bipolar skirtlike structure or from the halo seen in *HST* optical images. The lobes are relatively brighter in Q-band images than in N-band images.

The (deconvolved) size of the core appears to increase with increasing wavelength. When measured across the equatorial axis, the sizes of the core (FWHM) at different wavelengths are  $0''.261$  ( $10.38 \mu\text{m}$ ),  $0''.261$  ( $11.66 \mu\text{m}$ ),  $0''.279$  ( $12.5 \mu\text{m}$ ),  $0''.338$  ( $18.3 \mu\text{m}$ ), and  $0''.518$  ( $24.56 \mu\text{m}$ ). The consistency of these values suggests that the PSF was fairly stable throughout the observations. If the PSFs were truly stable, then the apparent increase of the core size

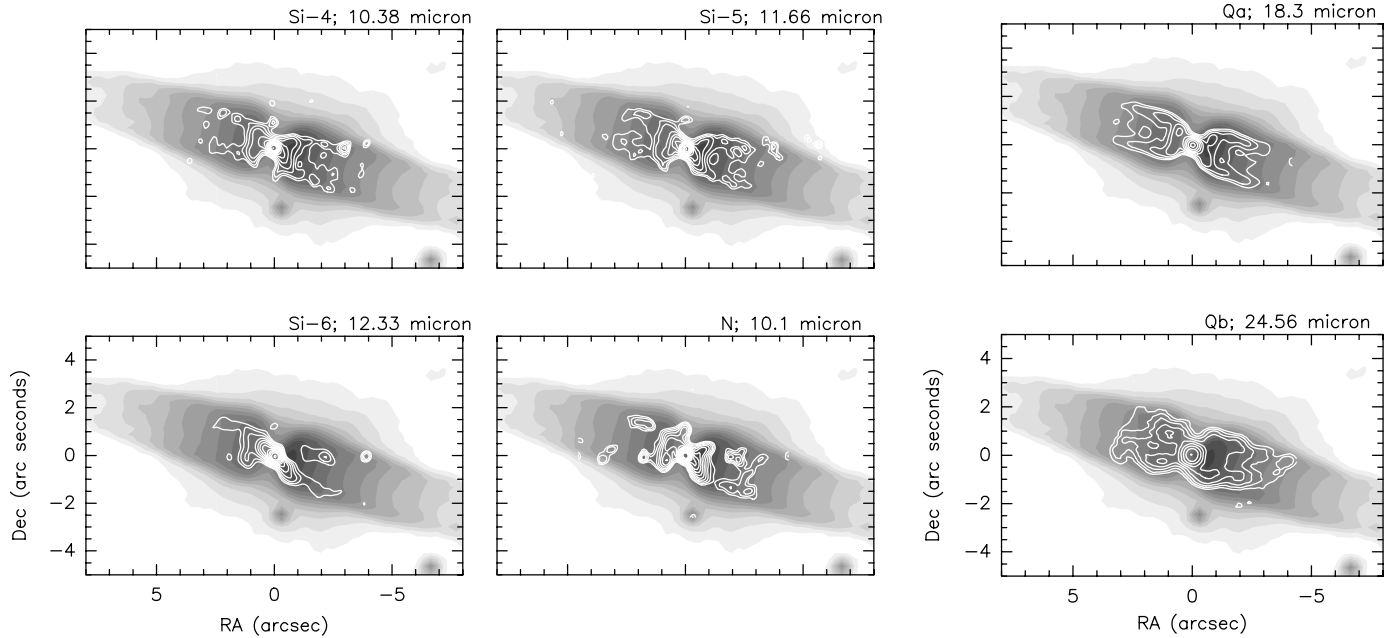


FIG. 2.—TRACS images (*contours*) superposed with the *HST* F606W image (*grayscale*). Both images are in logarithmic scale. For the TRACS image, the contour levels are in log (mJy pixel<sup>-1</sup>) from level 0.74 (5.47 mJy pixel<sup>-1</sup>; for N filter it is 0.44 [2.72 mJy pixel<sup>-1</sup>]) to 2.17 (148 mJy pixel<sup>-1</sup>) in step sizes of 0.13.

with wavelength could be interpreted as being due to the existence of a temperature gradient in the core.

The derived T-ReCS flux at 24.56  $\mu\text{m}$  is low in comparison to the *ISO* flux at that wavelength. This discrepancy is almost certainly due to atmospheric effects, as the Qb filter is much more sensitive to water vapor content than is the Qa filter or any of the *N*-band filters. As a result, we have scaled the Qb image flux to the *ISO* measurement at this wavelength, which is given in Table 1.

The *ISO* spectrum of Hen 401 shows that the T-ReCS flux for the Si-4, Qa and Qb filters are not contaminated by emission features and they represent the true continuum of the dust emission at 10.38  $\mu\text{m}$ , 18.3  $\mu\text{m}$ , and 24.56  $\mu\text{m}$ , respectively. Therefore, the color temperature distribution of dust can be obtained from the fluxes at these wavelengths for every pixel. For a dust cloud of uniform temperature, the ratio of emitted flux at two wavelengths  $\lambda_1$  and  $\lambda_2$  in the optically thin limit is

$$\frac{F_{\lambda_1}}{F_{\lambda_2}} = \left(\frac{\lambda_2}{\lambda_1}\right)^\alpha \frac{B_{\lambda_1}(T_d)}{B_{\lambda_2}(T_d)}, \quad (1)$$

where  $\alpha$  is the dust opacity index, and  $B_{\lambda_1}(T_d)$  and  $B_{\lambda_2}(T_d)$  are the Planck functions at  $\lambda_1$  and  $\lambda_2$  for dust temperature  $T_d$ . Fitting this function using the ratio  $F(10.38 \mu\text{m})/F(18.3 \mu\text{m})$  and the ratio  $F(18.3 \mu\text{m})/F(24.56 \mu\text{m})$  gives a best-fit  $T$  value of 275 K and  $\alpha = -1$  for the core, and  $T = 89$  K with  $\alpha = 0.45$  for the lobes. The fluxes at every pixel of the Si-4, Qa, and Qb filter images were fitted with the function  $F_\lambda \propto \lambda^{-\alpha} B_\lambda(T)$ , and the dust color temperature map of the nebula obtained by this method is shown in Figure 3.

The dust color temperature map (Fig. 3) clearly indicates a hot, spherical core at the center, which has an average temperature of 275 K (peak temperature of 385 K). Radial cuts of this map through the center, along both the equatorial and polar directions are shown in Figure 4. The core shows steep temperature gradients that can be fitted with straight lines of slopes 595 K arcsec<sup>-1</sup> and 580 K arcsec<sup>-1</sup> along the polar and equatorial directions, respectively. From Figure 3 we can also see that the tem-

peratures are enhanced along the walls of the lobes at  $\sim 90$  K, suggesting that the dust is warmed by interaction between the bipolar outflow and the surrounding circumstellar material. Most interestingly, two prominent arcs of temperature  $\sim 210$  K can be seen at equal distances from the core. These arcs could be the result of an outflow episode some time in the recent past.

We should add a note of caution that the color temperature map as presented in Figure 3 is not the same as dust temperature, because the source function (dust temperature) may vary with depth along the line of sight. The two parameters would be the same only in the case in which the dust-emitting region is both optically and geometrically thin, or completely optically thick (which will give the surface temperature).

### 3.1. Distribution of AIB Emission Features

A comparison between the *ISO* spectrum and the Si-5 filter profile indicates that most of the 11.3  $\mu\text{m}$  AIB emission feature flux

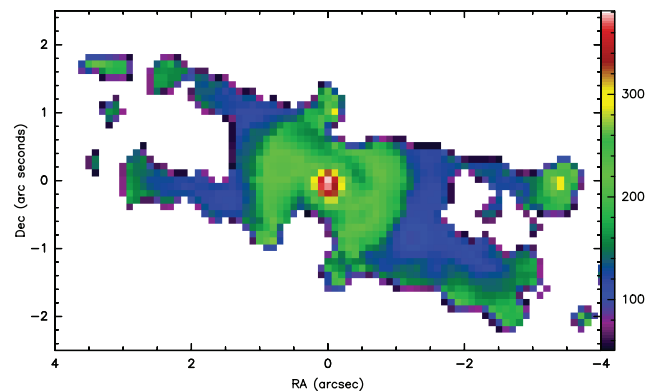


FIG. 3.—Color temperature map of dust emission in Hen 3-401 obtained by fitting modified blackbodies to the fluxes at every pixel of continuum images at 10.38  $\mu\text{m}$ , 18.3  $\mu\text{m}$ , and 24.56  $\mu\text{m}$ . The temperature scale corresponding to the false color map is given in the side bar.

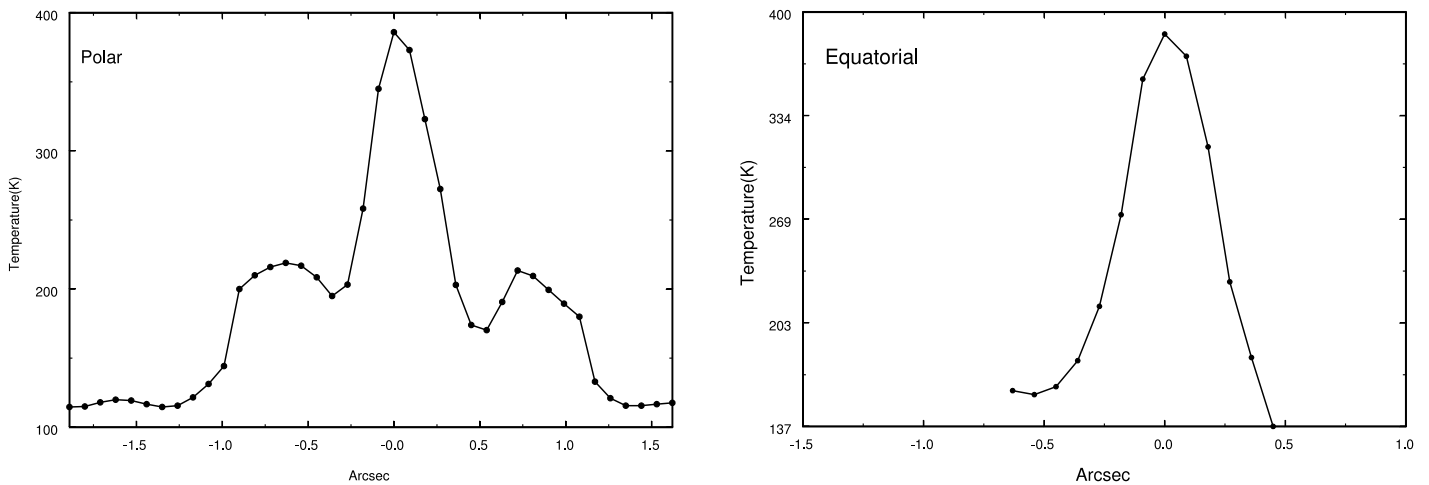


FIG. 4.—Radial cuts of the temperature map along polar (*left*) and equatorial (*right*) axes.

is received in this filter. Hence, the distribution of AIB emission features can be obtained by subtracting the  $11.66 \mu\text{m}$  continuum. The continuum at  $11.3 \mu\text{m}$  can be well approximated by the flux in the  $10.38 \mu\text{m}$  filter, and the continuum-subtracted image obtained in this way is shown in Figure 5. It can be seen from Figure 5 that the emission is distributed in the central region, of size  $\sim 1''$ , and in at least three sets of arcs in the bipolar lobes. The arcs in the southwest lobe and the two extreme arcs in the northeast lobe are not continuous. If we take that central region as the core, then the integrated  $11.33 \mu\text{m}$  emission feature flux from the central region is  $0.64 \text{ Jy}$  (with a peak value of  $0.042 \text{ Jy pixel}^{-1}$  at the center), which represents 86% of the total observed AIB emission. The remaining AIB emission is in the arcs.

If we fit the pairs of arcs with circles, we find that the outermost two arcs are co-centric. The center of the inner arc is shifted, and it coincides with the center of the bright core (presumably the position of the central star). Taking the distance to the nebula as 3 kpc (Bujarrabal & Bachiller 1991), we can estimate the ex-

pansion timescales of these arcs. The oldest ejection occurred  $\sim 39,200/V_{\text{exp}}$  yr ago, and the time intervals between subsequent ejections are constant at a value of  $\sim 10,800/V_{\text{exp}}$  yr. The expansion velocity of the nebula is usually assumed to be  $17 \text{ km s}^{-1}$ . However, since the inclination angle of the lobes is not known, the actual expansion velocity may be much higher. From the *HST* image, it appears that the nebula lies nearly on the plane of the sky. Taking a typical value of the lobe velocity in PPNs as  $\sim 80 \text{ km s}^{-1}$ , the timescales of the oldest ejection and the time interval between two subsequent ejections are 490 and 135 yr, respectively.

Figure 6 shows the AIB distribution superposed with the temperature map. We can see that the AIB emitting regions follow the regions where there is an enhancement in temperature, although there are regions where one sees a temperature enhancement but no AIB emission. Since the intensity is proportional to the Planck function and is highly dependent on temperature, the lack of AIB emission in some temperature-enhanced regions

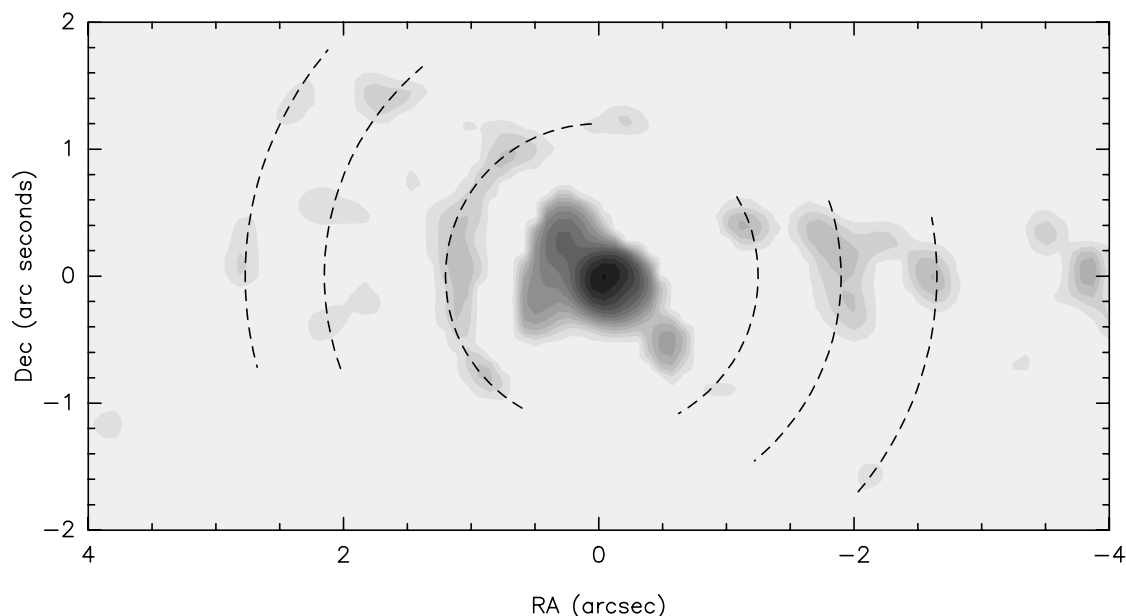


FIG. 5.—Continuum-subtracted  $11.66 \mu\text{m}$  image showing the distribution of the carrier of AIB emission. Partial circles are fitted for the observed arcs. The gray-scale map is presented in discrete levels in units of  $\log$  flux ( $\text{mJy}$ ) per pixel, from  $-1$  ( $0.1 \text{ mJy pixel}^{-1}$ ) to  $1.62$  ( $42 \text{ mJy pixel}^{-1}$ ) in step sizes of  $0.22$ .

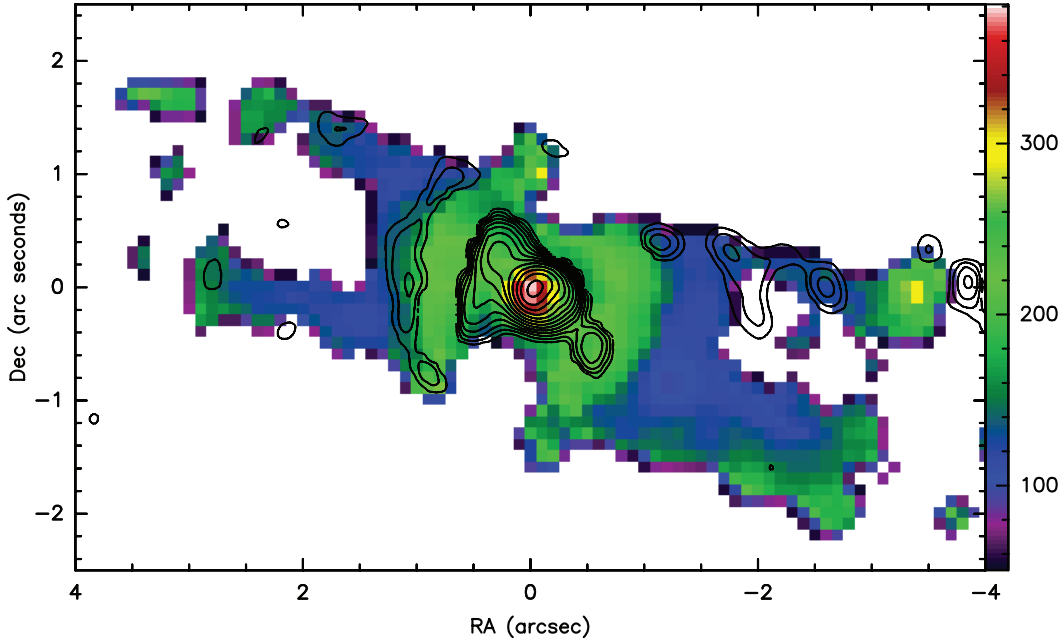


FIG. 6.—AIB distribution (*contour*) superposed with the dust color temperature map. AIB contour levels are in log (mJy pixel<sup>-1</sup>) from -1 (0.1 mJy pixel<sup>-1</sup>) to 1.62 (42 mJy pixel<sup>-1</sup>) in step sizes of 0.22.

suggests that the emission in the arcs is not due to temperature effects alone. The elimination of this effect after the continuum subtraction shows that the continuum is adequately removed from the 11.66  $\mu\text{m}$  image. The continuum-subtracted image therefore represents the distribution of the carrier of the AIB emission features. The arcs could imply that the star has undergone multiple ejections of the material from which the AIB carrier was synthesized. The enhancement of temperature could be caused by the shocks as this presumably fast-moving material interacts with the surrounding slower moving gas.

The derivation of the distribution of the AIB features can also be done by dividing the 11.66  $\mu\text{m}$  image by the 10.38  $\mu\text{m}$  image. Although such a division shows a distribution similar to that obtained by the subtraction, there is higher noise present in the deconvolved images. A division increases the residual noise, and so the distribution of emission features is not brought up clearly. It should be noted that for IRAS 07134+1005 and Z02229+6202, both PPNs showing strong 21  $\mu\text{m}$  features, the mid-IR imaging observations showed that there was no significant difference between the morphologies of continuum dust emission and the AIB emission features (Kwok et al. 2002).

### 3.2. Dust Mass

From the observed fluxes and derived color temperatures, we can in principle obtain the mass of the dust by (eq. [6.7], Kwok 2000)

$$M_d = \frac{F_\nu(16/3)\pi a \rho_s D^2}{Q_\nu B_\nu(T_d)}, \quad (2)$$

where  $F_\nu$  is the observed flux at frequency  $\nu$ ,  $a$  is the grain radius,  $Q_\nu$  is the grain absorption efficiency at frequency  $\nu$ ,  $\rho_s$  is the grain density, and  $B_\nu(T_d)$  is the Planck function at the dust temperature  $T_d$ . Assuming  $a = 0.5 \mu\text{m}$ ,  $Q_\nu = 0.1(\lambda/\mu\text{m})^{-\alpha}$ ,  $\alpha = 0.45$ ,  $\rho_s = 1 \text{ g cm}^{-3}$ ,  $T_d = 89 \text{ K}$  for the lobe, we have

$$M_d = 1.4 \times 10^{-3} (D/1 \text{ kpc})^2 M_\odot \quad (3)$$

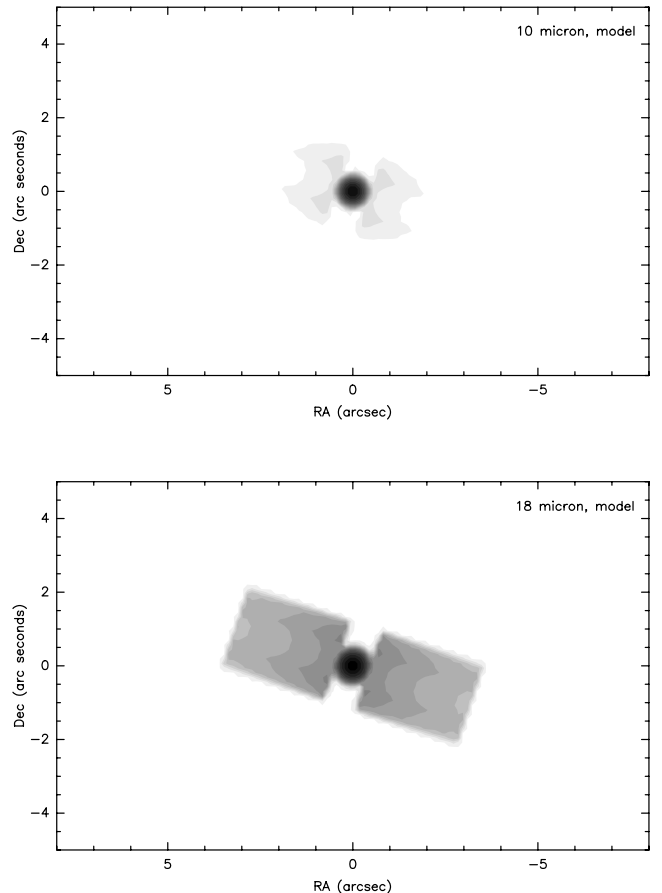


FIG. 7.—Model images at 10.38  $\mu\text{m}$  (*top*) and 18.3  $\mu\text{m}$  (*bottom*). See text for details of the model.

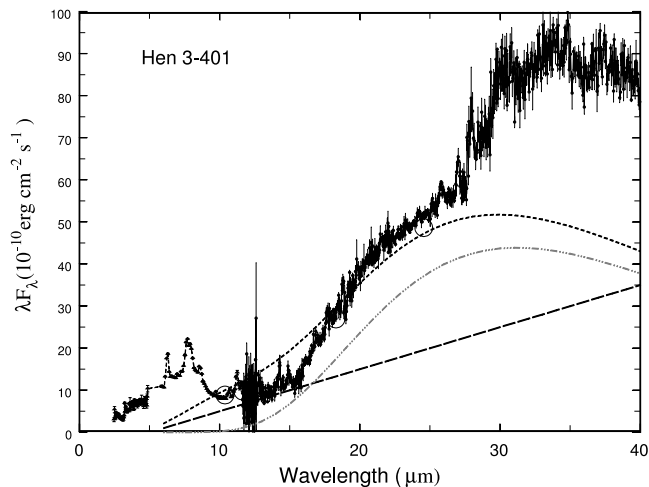


FIG. 8.—ISO SWS01 spectrum Hen 3-401 shown together with the model SED (dashed line, core; dot-dashed, lobes; dotted, total). The circles are TRCS fluxes. No attempt was made to model the AIB emissions.

for  $F_\nu = 8.81$  Jy at  $18.3 \mu\text{m}$ . The upper limit for the dust mass in the core can be obtained by setting  $\alpha = 0.45$ , and we have  $F_\nu = 7.6$  Jy at  $18.3 \mu\text{m}$  and  $T_d = 275$  K. This gives an estimate of  $3 \times 10^{-6} (D/1 \text{ kpc})^2 M_\odot$ .

The above derived dust masses in the lobes and the core from our infrared images can be compared to the total dust mass inferred from the *IRAS* measurements. Using the *IRAS*  $60 \mu\text{m}$  flux of 76.1 Jy and fitting the overall SED with a modified blackbody of  $\alpha = 0.7$  and  $T_d = 82$  K, we derived a total dust mass of  $5 \times 10^{-3} (D/1 \text{ kpc})^2 M_\odot$ . The amount of mass that is in the present infrared image, therefore, represents only 30% of the total dust mass, with the remaining probably too cold to be seen at  $20 \mu\text{m}$ . Assuming a typical gas-to-dust mass ratio of  $\sim 200$  for the circumstellar envelope, the total envelope mass is derived to be  $\sim 0.28 (D/1 \text{ kpc})^2 M_\odot$  in the lobes and  $\sim 1 (D/1 \text{ kpc})^2 M_\odot$  in total.

### 3.3. A Disk in the Core?

The fact that  $\alpha$  is negative instead of the normal value of  $\alpha \sim 1-2$  for micron-sized grains suggests that the temperature distribution in the core is not uniform. In such a case, the SED will depend on the density and temperature distribution of the dust. If the density distribution deviates from that of a spherical distribution, then the spectral shape will be a function of the geometry as well.

The SED of the circumstellar disks of young stellar objects has been well investigated in the literature. For example, the spectral index  $n = d \log F_\nu / d \log \nu$  for a flat, opaque, blackbody-like disk will have value of 0.33 (Lynden-Bell & Pringle 1974), whereas a flared disk in hydrostatic equilibrium will have  $n = -2/3$  (Chiang & Goldreich 1997). The similarity of this value with our observed spectral index for the core of Hen 3-401 suggests that emission from the core may be dominated by a flared disk.

### 3.4. Structure of the Lobes

Assuming a cylindrical geometry for the dust-emitting region in the lobes and a disk at the center, we have made model images for 10 and  $20 \mu\text{m}$  continuum emission in the optically thin limit. For the best-fit images, the cylinder has a length of  $14''$  and outer and inner radii  $r$  of  $1''.3$  and  $0''.7$ , respectively. The disk has a thickness of  $1''$  and radius of  $1''.3$ . The emissivity of the grain was taken as inversely proportional to the wavelength, and is taken to have a value of  $450 \text{ gm cm}^2$  at  $20 \mu\text{m}$ . The disk is assumed to follow a

density distribution of  $r^{-1}$ , whereas the density distribution along the cylindrical lobes is assumed to be as  $r^{-1.5}$ . The temperature at the lobes is assumed to be constant at 89 K, and in the disk the temperature distribution is approximated by  $T = [385 - 590(r/1'')] \text{ K}$ , according to the observed temperature profile in the core region. The inclination angle of the nebula is assumed to be  $0^\circ$ , as the nebula appears to lie almost on the plane of the sky. The computed model images are given in Figure 7, which are consistent with the observed continuum images at these wavelengths.

For comparison, we also plotted the model contributions of the disk and the lobes together with the observed SED in Figure 8. We note that the model does not explain the emission beyond  $30 \mu\text{m}$ . The long wavelength emission is likely to arise from colder dust outside the disk and the lobes detected in these observations.

We also note that this model is only a first approximation to study the effect of geometry on the dust emission image. A self consistent model will require the assumption of a central heating source and solution to the equation of transfer in axial symmetry (Spagna et al. 1991).

## 4. DISCUSSION

It is generally assumed that an accretion disk plays an important role collimating outflows in young stellar objects (YSOs) and active galactic nuclei (AGNs; Frank 1999). The discoveries of collimated outflows in bipolar and multipolar PNs (Sahai & Trauger 1998) have generated new interest in identifying the collimation mechanisms in evolved stars. While the equatorial disks in bipolar nebulae in the late stages of stellar evolution are often found to be expanding and are not necessarily accretion disks, it is widely believed that such disks play a role in collimating the fast outflows leading to morphological transformation of the nebulae. Compared to YSOs and AGNs, PPNs have the added advantage that the evolutionary and dynamical time scales are well known.

Equatorial disks in bipolar nebulae can be detected in many different ways: they appear as dark lanes in optical/near-IR images as the result of extinction of light from central stars; they manifest themselves in  $\text{H}_2$  emission caused by the large  $\text{H}_2$  column density at the equatorial regions; their dust emission can be imaged in the mid-infrared; the molecular content of the disks can be traced by rotational transitions of molecules such as CO; and the dust-scattered starlight can be imaged directly in the visible. An example of the last case is best illustrated by the collimated outflow coexisting with a disk and was first observed using *HST* in the PPN IRAS 17106 – 3046 (Kwok et al. 2000). Min 1-92 is a reflection bipolar nebula and is an example where collimated outflow is seen and is associated with a disk (Bujarrabal et al. 1998). Hen 3-401 is another example where the flared nature of the disk could have caused the highly collimated lobes as seen in *HST* optical and in our Gemini mid-IR observations. In such a flared disk one would expect the heating of dust grains at the flared edges of the disk and, hence the mid-IR emitting region should be extended. However, for disks that flare at intermediate radii but become too optically thin at large radii, the outer part of the disk can be shadowed, as found from the two-dimensional radiative transfer models of dusty disks (Dullemond 2002). This could possibly explain why such extended disk emission is not been observed in mid-IR.

## 5. CONCLUSIONS

We have obtained very high angular resolution mid-IR images of the bipolar nebula Hen 3-401. The images show a bright central core of size  $1''$  and extended emission along the walls of the

bipolar lobes. We also found the distribution of AIB emission features to be different from that of the continuum dust emission, and that the carrier of the AIB features may have been formed in multiple ejections. The core as imaged in the mid-infrared represents only a small fraction of total mass of the flared disk seen as a dark lane in *HST* optical images. The remaining dust is probably of low temperature and can only be observed in far-IR and submillimeter wavelengths. Hen 3-401 is therefore an example of the association of a flared disk with highly collimated outflows.

These observations demonstrate that thermally optimized, large, ground-based telescopes are capable of resolving the dust shells

of PPNs, which are essential to obtain complementary information on their structure and shaping mechanisms, as well as to find the distribution of the AIB emission feature carrier to understand how it is synthesized and excited.

This work was supported in part by grants to S. K. from the Natural Sciences and Engineering Research Council of Canada and by the National Science Council and Academia Sinica of Taiwan.

## REFERENCES

- Bujarrabal, V., Alcolea, J., Sahai, R., Zamorano, J., & Zijlstra, A. A. 1998, *A&A*, 331, 361
- Bujarrabal, V., & Bachiller, R. 1991, *A&A*, 242, 247
- Chiang, E. I., & Goldreich, P. 1997, *ApJ*, 490, 368
- Cohen, M., et al. 1999, *AJ*, 117, 1864
- Corradi, R. L. M. 2003, in *ASP Conf. Ser. 303, Symbiotic Stars Probing Stellar Evolution*, ed. R. L. M. Corradi, J. Mikolajewska, & T. J. Mahoney (San Francisco: ASP), 393
- Dullemond, C. P. 2002, *A&A*, 395, 853
- Frank, A. 1999, *NewA Rev.*, 43, 31
- García-Lario, P., Riera, A., & Manchado, A. 1999, *ApJ*, 526, 854
- Henize, K. G. 1976, *ApJS*, 30, 491
- Kwok, S. 2000, *The Origin and Evolution of Planetary Nebulae* (Cambridge: Cambridge Univ. Press)
- . 2003, in *ASP Conf. Ser. 303, Symbiotic Stars Probing Stellar Evolution*, ed. R. L. M. Corradi, J. Mikolajewska, & T. J. Mahoney (San Francisco: ASP), 428
- Kwok, S., Hrivnak, B. J., & Su, K. Y. L. 2000, *ApJ*, 544, L149
- Kwok, S., Volk, K., & Hrivnak, B. J. 2002, *ApJ*, 573, 720
- Loup, C., Forveille, T., Omont, A., & Paul, J. F. 1993, *A&AS*, 99, 291
- Lynden-Bell, D., & Pringle, J. E. 1974, *MNRAS*, 168, 603
- Parthasarathy, M., & Pottasch, S. R. 1989, *A&A*, 225, 521
- Parthasarathy, M., et al. 2001, *A&A*, 376, 941
- Sahai, R., Bujarrabal, V., & Zijlstra, A. 1999, *ApJ*, 518, L115
- Sahai, R., & Trauger, J. T. 1998, *AJ*, 116, 1357
- Sanduleak, N., & Stephenson, C. B. 1973, *ApJ*, 185, 899
- Scarrott, S. M., & Scarrott, R. M. J. 1995, *MNRAS*, 277, 277
- Silva, A. M., Azcarate, I. N., Poppel, W. G. L., & Likkell, L. 1993, *A&A*, 275, 510
- Spagna, G. F., Jr., Leung, C. M., & Egan, M. P. 1991, *ApJ*, 379, 232